PCP and Septins govern the polarized organization and mechanics of the actin cytoskeleton during convergent extension.

Caitlin C Devitt[1], Shinuo Weng[1], Vidal D Bejar-Padilla[1], José Alvarado[2], and John B Wallingford[1]

1. Department of Molecular Biosciences, University of Texas, Austin, TX 78712, USA.
2. Department of Physics, University of Texas, Austin, TX 78712, USA.

*To whom correspondence should be addressed:
Wallingford@austin.utexas.edu

Summary

Convergent extension (CE) is a collective cell movement required for embryonic axis elongation, neural tube closure, and kidney tubule elongation. During CE, iterative cell intercalations drive the elongation of a tissue [1]. In order to move, cells reorganize their actin cytoskeleton; the implication of actin regulators during CE, then, is expected. Interestingly, two other groups of proteins have been shown to be required for this cell behavior: Planar Cell Polarity proteins (PCP)[2-4] and Septins[5], both of which interact with the actin cytoskeleton [6-14]. Disruption of any of these systems have substantial overlap in terms of embryonic phenotypes, but how they interact to govern CE is largely unknown[15-17]. Here, we find that PCP proteins and Septins sequester actomyosin activity, create flows of actin across the anterior side of cells, and bundle actin into a node and cable system that displays a planar polarized gradient of stiffness.

Key findings:

- PCP- and Septin-dependent actin node and cable structures form and become anteriorized over time
- Actin cytoskeletal reorganization correlates with PCP protein polarization.
- Actomyosin flows are directed to anterior PCP puncta and PCP movement relies on actin turnover.
- Septins localize to anterior nodes and bundle actin filaments into anterior actin cable.
- PCP- and Septin-dependent anterior actin cables increase local cellular stiffness and create a planar polarized stiffness gradient across the cell.

Pioneering studies of vertebrate axis elongation demonstrated that isolated dorsal tissues of *Xenopus* gastrula undergo elongation autonomously [18, 19] through the collective cell movements of convergent extension (CE) [20-22]. Decades of study have now characterized changes to the cell shapes and behaviors that drive CE, and key insights came from the findings that planar cell polarity (PCP) signaling and actin regulation are essential [2, 16, 17, 23-27]. Loss of PCP signaling[6, 28] or actin regulators such as Cofilins, Wdr1, or Twinfilin [16, 17, 23, 24] perturbs essentially all sub-cellular behaviors associated with normal CE, while disruption of Septins elicits a more specific defect in CE-related cell behaviors [5, 29]. Despite these differences, the overall embryonic phenotypes are quite similar: each perturbation results in tissue-level defects in CE.

It is now clear that at least three distinct actin populations are essential for CE, including mediolaterally oriented actin-rich protrusions[21, 22, 28, 30], a contractile actomyosin network at deep cell-cell junctions [5, 31], and a superficial, cortical actomyosin meshwork referred to as the “node-and-cable” network [32-34]. Here, we delineate the spatiotemporal evolution of the node and cable network using time lapse and fluorescent actin speckle imaging, and we examine the role of core PCP proteins and Septins. We find that PCP controls the formation of actin nodes and cables and the orientation of actin filaments, while Sept7 controls only actin enrichment in the cable and modestly impacts node and cable positioning. This prompted a further exploration of PCP and Sept7 functions, revealing a key role in establishment of a subcellular mechanical gradient within the cortical actin cytoskeleton in cells engaged in CE. These data provide new insights into the control of actin systems and sub-cellular biomechanics of a central morphogenetic mechanism in vertebrate embryogenesis.

Progressive assembly of actin nodes and cables during CE

During CE, initially round cells extend protrusions that progressively align and stabilize at the mediolateral sides of cells; subsequently, cells elongate in the ML axis and intercalate between one another (Figure 1A). To understand how actin node-and-cables form within cells, we first examined the alignment and orientation of individual actin filaments throughout *Xenopus* gastrulation. At the onset of gastrulation, before cells polarize [21, 35] (NF Stage 11), we observed a random orientation of actin filaments (Figure 1B, hour 1). Over time, however, actin filaments aligned with the long axis as individual cells elongate (Figure1C-E, hour 2-4). Interestingly, instead of one proceeding the other, we identified a strong correlation between the cell elongation and alignment of actin filaments over time; they appear to progress simultaneously (Figure 1b''-e'', F).

We also noticed two additional features: first, actin node and cable structures were made up of many actin filaments; and second, these filaments were enriched at the anterior sides of cells, as shown through the AP localization of nodes over time (Figure 1G). To understand these two features, we looked at the localization of several proteins known to govern anteroposterior cell polarity and actin dynamics during *Xenopus* CE and found enrichment at actin nodes.

Specifically, to understand the asymmetry of the actin node and cable, we looked at the core anterior PCP proteins. Vangl2 and Prickle1 have been shown in zebrafish and mice to be present specifically in foci biased to the anterior side of cells engaged in CE [36-38]. We observed similar foci in the *Xenopus* dorsal marginal zone (DMZ), and these foci co-localized with the anteriorly positioned actin-rich nodes (Figure. 1H-J; Figure S1E-F). Moreover, the progressive polarization of Vangl2 and Prickle2 mirrored the progressive polarization of the actin node and cable system (Figure S1A-B, D-F, H). By contrast, the posterior core PCP protein Dishevelled was not present in actin nodes, but rather localized to posteriorly biased foci (Figure S1C-D, G-H).

We also observed strong localization in actin-rich nodes of several Septin subunits, the myosin light chain Myl9 [5], and the actin regulator cyclase-associated protein (CAP2)(Figure 1K-P). These results suggest that several proteins known to regulate actin during CE may work in concert in anterior actin-rich nodes.

PCP proteins and Septins govern distinct aspects of node and cable formation

We next asked if PCP signaling is required for actin node and cable formation. We disrupted PCP by Vangl2 knockdown (KD), Prickle 2 (Pk2) KD, or expression of dominant negative Disheveled (Xdd1) [6, 25], and we assessed the effect of PCP disruption on filament alignment using the method described above. Disruption of PCP signaling with any of these reagents randomized actin filament alignment (Figure. 2B-D, b'-d'). We then assayed the anterior localization of actin cables by plotting the intensity of the actin signal across the AP axis of individual cells (Figure. 2a''). This analysis revealed that disruption of PCP signaling also disrupted the anterior enrichment of actin filaments (Figure. 2b''-d'').

Loss of Septin function by knockdown of Sept7 strongly disrupts CE at the tissue level, but elicits a cellular phenotype that is far milder than PCP disruption (Figure. 2E)[29]. Accordingly, loss of Sept7 also elicited a milder effect on actin cables. Specifically, we observed no effect on the mediolateral alignment of actin filaments (Figure. 2e') though Sept7 KD *did* significantly disrupt the anterior enrichment of the cables (Figure. 2e''). These data suggested that loss of Sept7 may provide a point of entry from which to explore the specific organization of the node and cable system.

Sept7 controls local dynamics of polarized actin flows

We next turned to fluorescent speckle microscopy, by which mosaically labeled actin monomers are used to trace the movement of actin speckles within individual cells[24, 39-41]. Using Particle Imaging Velocimetry [42] to quantify actin flow, we observed a consistent pattern in which actin speckles flow along anterior actin cables into the anteriorly positioned nodes (Figure. 3A-C). More specifically, quantification of actin speckle flows shows actin movement is directed to PCP- and myosin-enriched nodes. For a more granular understanding of this actin flow, we used our speckle imaging data to trace *individual* actin speckles over time, measuring the lifetime of speckles in nodes and nearby cables independently (Figure. 3D). We found that the lifetime of actin speckles in nodes was significantly shorter than the lifetime of actin speckles incorporated in actin filaments within the anterior actin cable (Figure 3D). Thus, both the PIV and the analysis of individual speckles suggest that actin is highly dynamic in nodes and far less dynamic in nearby cables (Figure 3B&D).

Given its role in actin cable formation (Figure 2E, e"), we next asked if Sept7 controlled local actin dynamics in nodes and cable. We observed a very specific effect: Sept7 KD did not alter the shorter lifetime of actin speckles in nodes, but significantly reduced the longer actin speckle lifetimes observed in cables (Figure. 3D). Thus, Sept7 is required for the increased stability of actin filaments observed in anterior actin cables.

Sept7 is required for progressive actin cable bundling and anterior positioning of Vangl2

Septins have been shown to associate with and bundle actin filaments[9, 43, 44], so we used time-lapse imaging to define the evolution of the Sept7 KD phenotype during CE. We found that in control cells, actin filaments coalesce into a single actin- rich cable over time (Figure 3E). After Sept7 KD, however, this coalescence was severely disrupted, and instead actin filaments remained well spaced on average, even at late stages (Figure 3F, quantification Figure 3G). Thus, Sept7 controls both the local dynamics of actin monomers within cables and also the larger-scale bundling of actin filaments into anteriorly localized cable structures.

The core PCP protein Vangl2 is present in actin-rich nodes (Figure 1H-I, S1A, E, I-L), and actomyosin is well known to function both upstream and downstream of PCP proteins[5, 8, 45, 46]. We therefore reasoned that Sept7-dependent formation of the anterior actin cable might also affect Vangl2 polarization. Indeed, it did. Sept7 KD modestly, yet significantly, disrupted the normal planar polarized position of Vangl2+ foci in the anterior region of cells (Figure 3I-K). By contrast, Sept7 was dispensable for the actin-dependent mediolateral movement of Vangl2+ foci (Figure S2A-E).

Sept7 and Vangl2 are required to establish a subcellular, planar-polarized stiffness gradient in the actin cytoskeleton

Our data demonstrate an intricate relationship between Sept7, the core PCP proteins, and the actin node and cable system. Because our recent work with deep cell-cell junctions during CE has revealed a key role for very local, subcellular mechanical heterogeneity[31, 47, 48], we looked for similar heterogeneities conferred by the actin node and cable system during CE. To this end, we examined persistence length (L_p) of actin filaments, a basic mechanical property that reflects bending stiffness of a polymer, and this metric can be assayed simply from image data

[49, 50]. By segmenting LifeAct-GFP labeled actin from TIRF movies using SOAX software[51], we calculated the L_p [49]. We observed significantly higher persistence lengths for actin filaments in anterior actin cables compared to filaments in posterior regions (Figure 4A,D), suggesting distinct mechanical properties of the actin cytoskeleton in the anterior and posterior regions of cells engaged in CE. Strikingly, this stiffness pattern was eliminated by loss of Sept7 and Vangl2 (Figure 4A-F), where Sept7 KD and Vangl2 KD cells displayed reduced persistence lengths in the anterior and a lack of mechanical heterogeneity across anterior and posterior regions.

Discussion

PCP signaling has been linked to large scale morphogenetic movements in many tissues [2, 4, 52]. However, due to our limited understanding of the cellular and molecular mechanisms of this polarity system, its function remains mystifying. Here, we begin to tie this group of proteins to large scale cytoskeletal organization leading to a change in the local mechanical environment. We believe these data reveal a new layer to the function of PCP signaling during morphogenesis.

Specifically, our finding that PCP proteins in the mesenchyme localize to small, discrete puncta within actin-rich nodes led us to wonder how these protein complexes can have such a large effect on the cellular and tissue scales. We show also that in association with anterior PCP proteins, Septins bundle actin filaments into the anterior actin cable, increase the stability of actin filaments within the cable, and increase the subcellular stiffness of anterior sides of cells. Indeed, this behavior is consistent with known properties of actin-binding proteins, which slow down actin filament depolymerization, hence leading to stability[53], as well as increase the stiffness of the actin filament network[54]. Our analysis of the actin cytoskeleton has identified a downstream effect of PCP signaling, effecting the overall mechanical architecture of the cytoskeleton and leading to a planar polarized gradient of stiffness across the actin fibers within individual cells. The distinct change in mechanical environment in PCP and Septin morphants may account for the large scale embryonic phenotypes we have observed. We think these finding are informative on two levels: 1. This stiffness gradient leads to distinct mechanical

signals previously undetected, and 2. This distinct mechanical signal could be sensed by neighboring cells and impact the intercalation behavior of the cell collective.

Figure Legends:

Figure 1: Actin node and cable structures form and polarize over time, and actin-related proteins, anterior PCP proteins, and Septins localize to actin rich nodes
A) Schematic of individual cell shape change during CE. B) Individual cell mosaically labeled with Lifeact at hour 1. b') Orientation J labeling orientation of actin filaments, diagram of spokes correlating with angle LUTs. b") quantification of actin filament orientation. C) hour 2 D) hour 3) E) hour 4 showing alignment of filaments along the long axis (mediolateral cell axis), cyan box highlighting individual nodes in each cell, with inlay showing node morphology. b'-e') Orientation J LUT showing actin filament orientation. b"-e") quantification of actin filament orientation. F) Quantification of cell length to width ratios over time as cells elongated in the mediolateral axis (Hr1 n= 103 cells, Hr2 n=117 cells, Hr3 n=98 cells, Hr4 n=73 cells). G) Upper panel, schematic of AP localization, arrow representing cellular anterio-posterior axis. Lower panel, quantification of node positioning over time, (Hr1 n= 103 cells, Hr2 n=117 cells, Hr3 n=98 cells, Hr4 n=73 cells). H) Vangl2-GFP (green) expressed mosaically with Lifeact-RFP (magenta), showing punctate localization in actin rich node (cyan box). I) Vangl2 localization at a single node, i') actin rich node along actin cable, i") colocalization of Vangl2 and actin rich node. J, j', j") Pk2 K, k', k") Myl9 L, l', l") Sept2 M, m', m") Sept7 N, n', n") Sept8 O, o', o") Sept9. Scalebar = 10 um. See also Figure S1.

Figure 2: Actin node and cable formation and polarization requires PCP polarity and Septins
A) Control cell along with schematics of key features of actin cable. a'-e') schematic and measure of filament orientation a"-e") schematic and measure of anterior cable intensity showing loss of features in B) Vangl2 morphant (control vs Vangl2MO, Kolmogorov-Smirnov test, actin filament orientation $p<0.0001$; n= 38 control cells from 12 embryos; n=46 morphant cells from 13 embryos). C) Prickle 2 morphant (control vs Pk2MO, Kolmogorov-Smirnov test, actin filament orientation $p<0.0001$; n= 23 control cells from 4 embryos; n= 23 morphant cells from 4 embryos). D) dominant negative (DN) disheveled (Xdd1) (control vs Xdd1, Kolmogorov-Smirnov test, actin filament orientation $p<0.0001$; n=23 control cells from 13 embryos; n= 38 mutant cells from 8 embryos) and E) Sept7 morphant cells (control vs Sept7MO, Kolmogorov-Smirnov test, actin filament orientation $p=0.5596$; n= 26 control cells from 10 embryos; n= 31 morphant cells from 10 embryos). Scale= 10um.

Figure 3: Septins control local dynamics of polarized actin flows.
A) PIV analysis showing vectors of actin speckle trajectories with divergence LUT, cyan box highlighting PCP protein localization at actin node as imaged in a different channel, and B) zoomed in vectors and area of high negative divergence co-localizing with anterior PCP protein localization. C) quantification showing overlap of PCP protein localization and high negative divergence of actin speckle movement (n=7 control cells from 6 embryos). D) quantification of actin speckle lifetime at nodes vs surrounding cables (Kruskal-Wallis test, control node vs control cable $p=0.0093$, control node vs Sept7MO node ns $p>0.9999$, control cable vs Sept7MO cable $p<0.0001$, Sept7MO node vs Sept7MO cable $p>0.999$, control cable vs Sept7MO nodes $p=0.0033$, nodes vs Sept7MO cable n.s. $p=0.5498$; n= 31 control node, n=29 control cable from 12 embryos; n= 13 Sept7MO node, n= 19 Sept7MO cable from 7 embryos). E) actin cable bundling in control cells. F) actin filaments in Sept7 morphants showing lack of actin bundling. G) quantification of actin filament coalescence over time (control vs vangl2 MO, n=3 control cells; n= 3 Vangl2MO cells). H) Vangl2-GFP localization in control and I) Sept7MO cells, J) Quantification (Mann-Whitney test, control vs Sept7 MO, $p<0.0001$****, n=34 control cells from 3 embryos; n= 60 Sept7MO cells from 6 embryos). K) Schematic of Vangl2 localization (green) and anterior actin cables (magenta) in control and L) Sept7 morphant cells Scale= 10um.

Figure 4: PCP- and Septin-dependent anterior cable provides a subcellular stiffness gradient.
A) Representative TIRF image of a control cell, outlined in pink. Boxes highlighting anterior (cyan) and posterior (yellow) regions of the cell. B-G) Representative cropped ROIs as indicated from (B&C) control, (D&E) Sept7 morphants, and (F&G) Vangl2 morphant cells. b'-g') tSOAX segmentation and b"-g") representative single actin filament traces used for quantification of Lp. H) quantification of persistence length (Lp) of actin filaments in anterior (A) or posterior (P) cellular regions. Kruskal-Wallis test, (Control A vs P p=0.0046**, Sept7MO A vs P p>0.999 n.s., Vangl2 MO A vs P p>0.999 n.s., Control A vs Sept7MO A p=0.0481*, Control A vs Sept7MO P p= 0.0037**, all other pairwise comparisons p>0.999 n.s.)

Figure S1: Actin node and cable formation correlates with PCP polarity establishment
A-E) Pre-polarization localization of A) Vangl2-GFP B) Prickle 2-GFP and C) Dishevelled2-GFP. D) quantification pre-polarization showing random distribution of PCP proteins along the AP axis (Kruskal-Wallis, p>0.999 n.s., Vangl2 GFP n= 31 cells from 7 embryos; Pk2GFP n= 42 cells from 9 embryos; Dvl2-GFP n= 84 cells from 3 embryos), arrows pointing to GFP-tag. E-G) Polarized localization of E) Vangl2-GFP F) Prickle2-GFP and G) Dishevelled2-GFP. H) quantification showing anterior PCP proteins (Vang2 and Pk2) localize anteriorly and posterior PCP protein (Dvl2) localizes to the posterior (Kruskal-Wallis test; Vangl2 vs Pk2 p>0.999, Vangl2 vs Dvl2 p<0.0001, Pk2 vs Dvl2 p<0.0001; Vangl2 GFP n= 74 cells from 10 embryos; Pk2GFP n= 45 cells from 3 embryos; Dvl2-GFP n= 75 cells from 9 embryos). I) Endogenous staining of Vangl2 (Green), phalloidin (magenta), and DAPI (cyan). J) Experiment design highlighting mosaic knockdown of Vangl2 and staining for endogenous Vangl2 L) Endogenous staining for Vangl2, mosaic knockdown of Vangl2 traced in blue, arrowhead pointing to Vangl2 puncta. K) Quantification confirming mosaic knockdown of Vangl2.

Figure S2: Actin turnover is required for mediolateral movement of anterior PCP proteins while Septins are dispensable
A) Kymograph of Pk2 mediolateral movements over time. B) Pk2 movement +blebbistatin (50uM) C) Pk2 movement +LatB (1uM) D) Pk2 movement +Sept7MO E) quantification (Kruskal-Wallis test; control vs blebb p<0.0001, control vs LatB p=0.005, control vs Sept7 morphant p=0.888, blebb vs LatB p>0.999 n.s., blebb vs Sept7MO p>0.999 n.s., LatB vs Sept7MO p>0.999 n.s.). Scale= 10um.

Methods

Key resources table

REAGENT or RESOURCE	SOURCE	IDENTIFIER
Antibodies		
Rat anti-Vangl2 antibody (GST-tagged recombinant Vangl2 N-term fragment)	Millipore-Sigma	MABN750
Chemicals, peptides, and recombinant proteins		
hCG (human chorionic gonadotropin)	Merck	Code# 133754
Alexa 647 conjugated Actin	ThermoFisher	Cat# A12374
Latrunculin B	Abcam	Cat# ab144291
(S)-nitro-Blebbistatin	Cayman Chemicals	Item No. 13891
Critical commercial assays		
mMessage mMachine SP6 transcription kit	ThermoFisher	Cat# AM1340
Oligonucleotides		
Vangl2 morpholino	Park & Moon[55]	Gene-tools.com
Pk2 morpholino	Butler & Wallingford[56]	Gene-tools.com
Septin 7 morpholino	Kim et al[29]	Gene-tools.com
Recombinant DNA		
Lifeact-RFP	Riedl, et al. [57]	N/A
Vangl2-GFP	Butler & Wallingford[56]	N/A
Pk2-GFP	Butler & Wallingford[56]	N/A
Dvl2-GFP	Wallingford, et al.[28]	N/A
Septin7-GFP	Becker-Heck, et al.[58], Shindo & Wallingford[5]	N/A
Septin2-GFP	Becker-Heck, et al.[58], Shindo & Wallingford[5]	N/A
SF9-mNeon	Vielemeyer, et al.[59]	N/A
CAP1-GFP	Devitt, et al.[24]	N/A
DN Dishevelled (Xdd1)	Wallingford, et al.[28]	N/A
Software and algorithms		
FIJI	Schneider et al.[60]	Fiji.sc
Prism	GraphPad Software	Graphpad.com
Excel	Microsoft	Microsoft.com
Matlab	MathWorks	Mathworks.com
Python	Python	Python.org
Orientation J	Püspöki, et al.[61]	http://bigwww.epfl.ch/demo/orientation/
MosaicSuite	Sbalzarini & Koumoutsakos[62]	http://mosaic.mpi-cbg.de
TSOAX v0.1.8	Xu, et al.[63]	https://www.lehigh.edu/~div206/tsoax/

Lead contact

Further information and reagent requests should be directed to John B. Wallingford (Wallingford@austin.utexas.edu).

Material availability

All reagents available from lead contact with completed MTA upon request.

Data and code availability

Any additional information required to reanalyze the data reported in this paper is available from the lead contact upon request.

Data
All data reported in this paper will be shared by the lead contact upon request.

Code
This paper does not report original code.

Experimental model and subject details

Xenopus embryo manipulations:
Xenopus laevis females were super-ovulated by injection of hCG (human chorionic gonadotropin). The following day, eggs were squeezed from the females. In vitro fertilization was performed by homogenizing a small part of a harvested testis in 1X Marc's Modified Ringer's (MMR) and mixing with collected eggs. Embryos were dejellied in 3% cysteine (pH 7.9) at the two-cell stage. Fertilized embryos were rinsed and reared in 1/3X Marc's Modified Ringer's (MMR) solution. For microinjections, embryos were placed in a 2% ficoll in 1/3X MMR solution and injected using forceps and an Oxford universal micromanipulator. Morpholino oligonucleotide or CRISPR/Cas9 was injected into two dorsal blastomeres to target the dorsal marginal zone (DMZ). Embryos were microinjected with mRNA at the 4-cell stage for uniform labeling and at the 64- to 128- cell stage for mosaic labeling. Embryos were staged according to Nieuwkoop and Faber (Nieuwkoop and Faber, 1994). All animal work has been approved by the IACUC of UT, Austin, protocol no. AUP-2021-00167.

Method details

Plasmids, mRNA, protein, and MOs for microinjections:
Xenopus gene sequences were obtained from Xenbase (www.xenbase.org) and open reading frames (ORF) of genes were amplified from the *Xenopus* cDNA library by polymerase chain reaction (PCR), and then are inserted into a pCS10R vector fused with C-terminal GFP. The following constructs were cloned into pCS vector: Sept8-GFP, Sept9-GFP. These constructs were linearized and the capped mRNAs were synthesized using mMESSAGE mMACHINE SP6 transcription kit (ThermoFisher Scientific, Waltham, MA, USA). Concentration for GFP localization was titrated to lowest concentration where we could still detect GFP signal, but no cellular phenotype was observed. The amount of injected mRNAs per blastomere are as follows: Lifeact-GFP or –RFP [50-100pg], Pk2-GFP [35pg][6], Vangl2-GFP [35pg][6], Dvl2-GFP [5-8pg][28], SF9-GFP [25pg][59], Cap1-GFP[25pg] , Septin2- GFP [50pg][29], Septin7-GFP [35pg][5, 58], Septin8-GFP [40pg], Septin9GFP [40pg] and Xdd1 [500pg][28].

Morpholinos:
Morpholinos used were previously designed to target exon-intron splicing junction (Gene Tools, Philomath, OR, USA). The MO sequences and the working concentrations include: Septin7 morpholino[5, 29, 64], 5' TGCTGTAGAGTCAGTGCCTCGCCTT 3', 40 ng per injection at 4-cell stage; Vangl2 morpholino[55], 5' CGTTGGCGGATTTGGGTCCCCCCGA 3', 20ng per injection at 4-cell stage; Pk2 morpholino[56], 5' GAACCCAAACAAACACTTACCTGTT 3', 20ng per injection at 4-cell stage.

Actin Speckle Microscopy:
For fluorescent actin speckle microscopy, labeled actin monomers (Alexa 568 conjugated Actin, Catalog number A12374, ThermoFisher, Waltham, MA, USA) were reconstituted in a 2mg/ml stock solution. A 0.01ug/ul working solution was prepared for each 10nl injection, and 0.1ng was injected into dorsal blastomeres of 4-cell stage embryos. This concentration was

determined empirically by titrating the amount injected until no cellular phenotype was observed and labeled actin monomers were sparse enough to detect individual "speckles" [40].

Live imaging of Keller explants:
mRNAs were injected at the dorsal side of 4 cell stage embryos, and the dorsal marginal zone (DMZ) tissues were dissected out at stage 10.5 using forceps, hairloops, and eyebrow hair knives. Each explant was mounted to a fibronectin-coated dish in Steinberg's solution[5], and cultured at 16℃ for half a day before imaging with a Zeiss LSM700 confocal microscope (Jena, Germany), or Nikon N-STORM combined TIRF/STORM microscope (Minato City, Tokyo, Japan).

Inhibitor treatments:
Inhibitors were solubilized in DMSO to a stock concentration of 10mM for Latrunculin B and 100mM for (+) Blebbistatin. Explants with labeled actin and Vangl2 were treated with 1uM LatrunculinB (diluted 1:10,000 in Steinberg's solution)(CAS Number: 76343-94-7), a cell permeable actin polymerization inhibitor, or100uM (+) Blebbistatin (diluted 1:1,000 in Steinberg's solution)(CAS Number 856925-75-2), a non-muscle myosin inhibitor. Samples were treated with DMSO (vehicle control) or specific inhibitors and imaged immediately after application.

Image analysis:
Images were processed with the Fiji distribution of ImageJ and Photoshop (Adobe) software suites, and figures were assembled in Illustrator (Adobe). Cell length and width measurements were manually taken in Fiji along the long axis and through the centroid of the cell. Similarly, AP positioning of node and PCP proteins across AP axis of cell, and anterior cable intensity were taken through the midline of the cell manually using intensity plots in Fiji. The displacement of PCP proteins and actin cable coalescence measurements were taken using kymographs and manual measurements between two points in Fiji.

Actin cable orientations were taken from TIRF images using the OrientationJ plugin in Fiji [61] (http://bigwww.epfl.ch/demo/orientation/).

Divergence measurements of actin speckles were taken using the PIVlab[42] software in Matlab.

Fluorescent actin speckle lifetime: measurements were taken by tracking individual speckles using MosaicSuite[62] (http://mosaic.mpi-cbg.de) object tracking plugin in Fiji. Custom scripts were written in Matlab to count the lifetime of each speckle.

Actin cable bundling: kymographs were taken across the anteroposterior axis of individual cells near the actin node. We then measured the distance between adjacent actin filaments over time over specified time intervals.

Persistence length measurements of actin filaments:
The open-source biopolymer tracking software TSOAX v0.1.8[63] (https://www.lehigh.edu/~div206/tsoax/) was used to automate actin fiber labeling of TIRF movies. The ridge threshold, stretch-factor, and gaussian std (pixels) parameters were set to 0.01, 1.5, and 1 respectively. These values were chosen as they resulted in accurate filament labeling. Remaining parameters were unchanged from default values. TIRF movies were processed prior to TSOAX analysis with the application of a gaussian blur of sigma radius = 1 to enhance accuracy of fiber tracking. TSOAX output containing the spatial and temporal coordinates that define labeled fibers and track groupings was imported into python. Fiber

coordinate data was used to calculate the length (l_n) and angle of each segment defining the fiber relative to the first segment (θ_n). Sum of fiber segment lengths defined total fiber length (L_t). Average correlation is defined by the following equation, where n is equal to the number of segments in a given snake:

$$< cos\theta_n > = \frac{\Sigma \cos\theta_0 + \cos\theta_1 + \cos\theta_2 + \cdots}{n}$$

Average correlation and total length were then used to calculate the persistence length of each fiber according to the following equation:

$$l_p = \frac{-L_t}{\ln(< cos\theta >)}$$

Average track persistence length $l_{p_{track}}$ was obtained by averaging all persistence length values of fibers in the same track grouping.

Quantification and statistical analysis:
Statistical analyses were carried out using Microsoft Excel, Matlab (Natick, MA, USA), and GraphPad Prism (Graphpad, San Diego, CA, USA) software. Each experiment was conducted on multiple days and included biological replicates. Due to non-normality observed and low n-number in some observations, we used non-parametric tests for statistical comparisons throughout the manuscript. We used Mann Whitley U tests, Kruskal-Wallis tests, or Kolmogorov–Smirnov tests for statistical comparisons of two groups, multiple groups, or distributions, respectively.

Data and code availability
All data reported in this paper will be shared by the lead contact upon request.

Acknowledgements
We would like to acknowledge the Microscopy and Imaging Facility of the Center for Biomedical Research Support at The University of Texas at Austin for use of equipment and specifically thank Anna Webb and Julie Hayes for assistance and technical expertise. And a big thank you to all of the members of the Wallingford lab for their advice and critical feedback!

Author contributions
C.C.D. and J.B.W. conceived the project. C.C.D., J.B.W., and J.A. designed the experiments. C.C.D. preformed all imaging and analysis, with assistance in persistence length analysis from S.W. and V.B.P. with supervision from J.A. C.C.D and J.B.W. wrote the paper with input and editing from all authors. Funding acquisition from J.B.W.

Declaration of interests
The authors declare no completing interests.

REFERENCES CITED

1. Tada M, Heisenberg CP. Convergent extension: using collective cell migration and cell intercalation to shape embryos. Development. 2012;139(21):3897-904. doi: 10.1242/dev.073007. PubMed PMID: 23048180.
2. Butler MT, Wallingford JB. Planar cell polarity in development and disease. Nat Rev Mol Cell Biol. 2017;18(6):375-88. doi: 10.1038/nrm.2017.11. PubMed PMID: 28293032.
3. Devenport D. The cell biology of planar cell polarity. J Cell Biol. 2014;207(2):171-9. Epub 2014/10/29. doi: 10.1083/jcb.201408039. PubMed PMID: 25349257; PMCID: PMC4210441.
4. Davey CF, Moens CB. Planar cell polarity in moving cells: think globally, act locally. Development. 2017;144(2):187-200.
5. Shindo A, Wallingford JB. PCP and septins compartmentalize cortical actomyosin to direct collective cell movement. Science. 2014;343(6171):649-52. doi: 10.1126/science.1243126. PubMed PMID: 24503851; PMCID: PMC4167615.
6. Butler MT, Wallingford JB. Spatial and temporal analysis of PCP protein dynamics during neural tube closure. Elife. 2018;7. Epub 2018/08/07. doi: 10.7554/eLife.36456. PubMed PMID: 30080139; PMCID: PMC6115189.
7. McGreevy EM, Vijayraghavan D, Davidson LA, Hildebrand JD. Shroom3 functions downstream of planar cell polarity to regulate myosin II distribution and cellular organization during neural tube closure. Biol Open. 2015;4(2):186-96. doi: 10.1242/bio.20149589. PubMed PMID: 25596276; PMCID: PMC4365487.
8. Nishimura T, Honda H, Takeichi M. Planar cell polarity links axes of spatial dynamics in neural-tube closure. Cell. 2012;149(5):1084-97. Epub 2012/05/29. doi: S0092-8674(12)00525-9 [pii] 10.1016/j.cell.2012.04.021. PubMed PMID: 22632972.
9. Mavrakis M, Azou-Gros Y, Tsai F-C, Alvarado J, Bertin A, Iv F, Kress A, Brasselet S, Koenderink GH, Lecuit T. Septins promote F-actin ring formation by crosslinking actin filaments into curved bundles. Nature cell biology. 2014;16(4):322.
10. Spiliotis ET, Nakos K. Cellular functions of actin- and microtubule-associated septins. Current Biology. 2021;31(10):R651-R66. doi: https://doi.org/10.1016/j.cub.2021.03.064.
11. Spiliotis ET. Spatial effects - site-specific regulation of actin and microtubule organization by septin GTPases. J Cell Sci. 2018;131(1). Epub 20180111. doi: 10.1242/jcs.207555. PubMed PMID: 29326311; PMCID: PMC5818061.
12. Martins CS, Taveneau C, Castro-Linares G, Baibakov M, Buzhinsky N, Eroles M, Milanović V, Iv F, Bouillard L, Llewellyn A, Gomes M, Belhabib M, Kuzmić M, Verdier-Pinard P, Lee S, Badache A, Kumar S, Chandre C, Brasselet S, Rico F, Rossier O, Koenderink GH, Wenger J, Cabantous S, Mavrakis M. Human septins in cells organize as octamer-based filaments mediating actin-membrane anchoring. bioRxiv. 2022:2022.02.23.481653. doi: 10.1101/2022.02.23.481653.
13. Eaton S, Wepf R, Simons K. Roles for Rac1 and Cdc42 in planar polarization and hair outgrowth in the wing of Drosophila. J Cell Biol. 1996;135(5):1277-89.
14. Winter CG, Wang B, Ballew A, Royou A, Karess R, Axelrod JD, Luo L. Drosophila Rho-associated kinase (Drok) links Frizzled-mediated planar cell polarity signaling to the actin cytoskeleton. Cell. 2001;105(1):81-91. PubMed PMID: 11301004.
15. Blair A, Tomlinson A, Pham H, Gunsalus KC, Goldberg ML, Laski FA. Twinstar, the Drosophila homolog of cofilin/ADF, is required for planar cell polarity patterning. Development. 2006;133(9):1789-97. doi: 10.1242/dev.02320. PubMed PMID: 16571634.
16. Luxenburg C, Heller E, Pasolli HA, Chai S, Nikolova M, Stokes N, Fuchs E. Wdr1-mediated cell shape dynamics and cortical tension are essential for epidermal planar cell polarity. Nat Cell Biol. 2015;17(5):592-604. Epub 2015/04/29. doi: 10.1038/ncb3146. PubMed PMID: 25915128; PMCID: PMC4523270.
17. Mahaffey JP, Grego-Bessa J, Liem KF, Jr., Anderson KV. Cofilin and Vangl2 cooperate in the initiation of planar cell polarity in the mouse embryo. Development. 2013;140(6):1262-71. Epub 2013/02/15. doi: 10.1242/dev.085316. PubMed PMID: 23406901; PMCID: PMC3585660.
18. Schectman AM. The mechanics of amphibian gastrulation. Univ Calif Pub Zool. 1942;51:1-39.
19. Holtfreter J. A study of the mechanics of gastrulation, Part II. J Exp Zool. 1944;95(3):171-212.
20. Keller R, Hardin J. Cell behaviour during active cell rearrangement: evidence and speculations. J Cell Sci Suppl. 1987;8:369-93.
21. Shih J, Keller R. Cell motility driving mediolateral intercalation in explants of Xenopus laevis. Development. 1992;116(4):901-14.
22. Wilson P, Keller R. Cell rearrangement during gastrulation of Xenopus: direct observation of cultured explants. Development. 1991;112(1):289-300.
23. Grego-Bessa J, Hildebrand J, Anderson KV. Morphogenesis of the mouse neural plate depends on distinct roles of cofilin 1 in apical and basal epithelial domains. Development. 2015;142(7):1305-14. Epub 2015/03/07. doi: 10.1242/dev.115493. PubMed PMID: 25742799; PMCID: PMC4378245.
24. Devitt CC, Lee C, Cox RM, Papoulas O, Alvarado J, Shekhar S, Marcotte EM, Wallingford JB. Twinfilin1 controls lamellipodial protrusive activity and actin turnover during vertebrate gastrulation. J Cell Sci. 2021;134(14). Epub 2021/06/02. doi: 10.1242/jcs.254011. PubMed PMID: 34060614; PMCID: PMC8325956.

25. Wallingford JB, Rowning BA, Vogeli KM, Rothbächer U, Fraser SE, Harland RM. Dishevelled controls cell polarity during Xenopus gastrulation. Nature. 2000;405:81-5.
26. Heisenberg C-P, Tada M, Rauch G-J, Saude L, Concha ML, Geisler R, Stemple DL, Smith JC, Wilson SW. Silberblick/Wnt11 activity mediates convergent extension movements during zebrafish gastrulation. Nature. 2000;405:76-81.
27. Tada M, Smith JC. Xwnt11 is a target of Xenopus Brachyury: regulation of gastrulation movements via dishevelled, but not through the canonical Wnt pathway. Development. 2000;127(10):2227-38.
28. Wallingford JB, Rowning BA, Vogeli KM, Rothbacher U, Fraser SE, Harland RM. Dishevelled controls cell polarity during Xenopus gastrulation. Nature. 2000;405(6782):81-5. doi: 10.1038/35011077. PubMed PMID: 10811222.
29. Kim SK, Shindo A, Park TJ, Oh EC, Ghosh S, Gray RS, Lewis RA, Johnson CA, Attie-Bittach T, Katsanis N, Wallingford JB. Planar Cell Polarity Acts Through Septins to Control Collective Cell Movement and Ciliogenesis. Science. 2010;329:1337-40. Epub 2010/07/31. doi: science.1191184 [pii]
10.1126/science.1191184. PubMed PMID: 20671153.
30. Keller R, Cooper MS, Danilchik M, Tibbetts P, Wilson PA. Cell intercalation during notochord development in Xenopus laevis. J Exp Zool. 1989;251(2):134-54.
31. Weng S, Huebner RJ, Wallingford JB. Convergent extension requires adhesion-dependent biomechanical integration of cell crawling and junction contraction. Cell Rep. 2022;39(4):110666. doi: 10.1016/j.celrep.2022.110666. PubMed PMID: 35476988.
32. Skoglund P, Rolo A, Chen X, Gumbiner BM, Keller R. Convergence and extension at gastrulation require a myosin IIB-dependent cortical actin network. Development. 2008;135(14):2435-44. Epub 2008/06/14. doi: dev.014704 [pii]
10.1242/dev.014704. PubMed PMID: 18550716.
33. Kim H, Davidson L. Methods to investigate molecular mechanisms and cellular mechanics responsible for moprhogenesis in Xenopus. In: Sharpe J, Wong RO, editors. Imaging in developmental biology: CSHL Press; 2011. p. 551-68.
34. Pfister K, Shook DR, Chang C, Keller R, Skoglund P. Molecular model for force production and transmission during vertebrate gastrulation. Development. 2016;143(4):715-27. doi: 10.1242/dev.128090. PubMed PMID: 26884399; PMCID: PMC4760319.
35. Shih J, Keller R. Patterns of cell motility in the organizer and dorsal mesoderm of Xenopus laevis. Development. 1992;116(4):915-30.
36. Ciruna B, Jenny A, Lee D, Mlodzik M, Schier AF. Planar cell polarity signalling couples cell division and morphogenesis during neurulation. Nature. 2006;439(7073):220-4. PubMed PMID: 16407953.
37. Yin C, Kiskowski M, Pouille PA, Farge E, Solnica-Krezel L. Cooperation of polarized cell intercalations drives convergence and extension of presomitic mesoderm during zebrafish gastrulation. J Cell Biol. 2008;180(1):221-32. Epub 2008/01/16. doi: jcb.200704150 [pii]
10.1083/jcb.200704150. PubMed PMID: 18195109; PMCID: 2213609.
38. Yang W, Garrett L, Feng D, Elliott G, Liu X, Wang N, Wong YM, Choi NT, Yang Y, Gao B. Wnt-induced Vangl2 phosphorylation is dose-dependently required for planar cell polarity in mammalian development. Cell Research. 2017;27(12):1466-84. doi: 10.1038/cr.2017.127.
39. Waterman-Storer CM, Desai A, Bulinski JC, Salmon E. Fluorescent speckle microscopy, a method to visualize the dynamics of protein assemblies in living cells. Current biology. 1998;8(22):1227-S1.
40. Watanabe N, Mitchison TJ. Single-molecule speckle analysis of actin filament turnover in lamellipodia. Science. 2002;295(5557):1083-6. Epub 2002/02/09. doi: 10.1126/science.1067470. PubMed PMID: 11834838.
41. Salmon ED, Waterman CM. How we discovered fluorescent speckle microscopy. Molecular biology of the cell. 2011;22(21):3940-2. doi: 10.1091/mbc.E11-07-0646. PubMed PMID: 22039068.
42. Thielicke W, Stamhuis E. PIVlab–towards user-friendly, affordable and accurate digital particle image velocimetry in MATLAB. Journal of open research software. 2014;2(1).
43. Smith C, Dolat L, Angelis D, Forgacs E, Spiliotis ET, Galkin VE. Septin 9 Exhibits Polymorphic Binding to F-Actin and Inhibits Myosin and Cofilin Activity. J Mol Biol. 2015;427(20):3273-84. Epub 20150819. doi: 10.1016/j.jmb.2015.07.026. PubMed PMID: 26297986; PMCID: PMC4587343.
44. Dolat L, Hunyara JL, Bowen JR, Karasmanis EP, Elgawly M, Galkin VE, Spiliotis ET. Septins promote stress fiber-mediated maturation of focal adhesions and renal epithelial motility. J Cell Biol. 2014;207(2):225-35. doi: 10.1083/jcb.201405050. PubMed PMID: 25349260; PMCID: PMC4210437.
45. Habas R, Dawid IB, He X. Coactivation of Rac and Rho by Wnt/Frizzled signaling is required for vertebrate gastrulation. Genes Dev. 2003;17(2):295-309.
46. Ybot-Gonzalez P, Savery D, Gerrelli D, Signore M, Mitchell CE, Faux CH, Greene ND, Copp AJ. Convergent extension, planar-cell-polarity signalling and initiation of mouse neural tube closure. Development. 2007;134(4):789-99. PubMed PMID: 17229766.
47. Huebner RJ, Malmi-Kakkada AN, Sarıkaya S, Weng S, Thirumalai D, Wallingford JB. Mechanical heterogeneity along single cell-cell junctions is driven by lateral clustering of cadherins during vertebrate axis

elongation. Elife. 2021;10. Epub 20210525. doi: 10.7554/eLife.65390. PubMed PMID: 34032216; PMCID: PMC8205493.
48. Huebner RJ, Weng S, Lee C, Sarıkaya S, Papoulas O, Cox RM, Marcotte EM, Wallingford JB. ARVCF catenin controls force production during vertebrate convergent extension. Dev Cell. 2022;57(9):1119-31.e5. Epub 20220426. doi: 10.1016/j.devcel.2022.04.001. PubMed PMID: 35476939.
49. Lamour G, Kirkegaard JB, Li H, Knowles TPJ, Gsponer J. Easyworm: an open-source software tool to determine the mechanical properties of worm-like chains. Source Code for Biology and Medicine. 2014;9(1):16. doi: 10.1186/1751-0473-9-16.
50. Wisanpitayakorn P, Mickolajczyk KJ, Hancock WO, Vidali L, Tüzel E. Measurement of the Persistence Length of Cytoskeletal Filaments using Curvature Distributions. bioRxiv. 2018:252551. doi: 10.1101/252551.
51. Xu Y, Cao J, Huang S, Feng D, Zhang W, Zhu X, Yan X. Characterization of tetratricopeptide repeat-containing proteins critical for cilia formation and function. PLoS One. 2015;10(4):e0124378. doi: 10.1371/journal.pone.0124378. PubMed PMID: 25860617; PMCID: PMC4393279.
52. Gray RS, Roszko I, Solnica-Krezel L. Planar cell polarity: coordinating morphogenetic cell behaviors with embryonic polarity. Dev Cell. 2011;21(1):120-33. Epub 2011/07/19. doi: S1534-5807(11)00245-0 [pii] 10.1016/j.devcel.2011.06.011. PubMed PMID: 21763613; PMCID: 3166557.
53. Schmoller KM, Semmrich C, Bausch AR. Slow down of actin depolymerization by cross-linking molecules. J Struct Biol. 2011;173(2):350-7. Epub 20100909. doi: 10.1016/j.jsb.2010.09.003. PubMed PMID: 20832473.
54. Lieleg O, Claessens MMAE, Bausch AR. Structure and dynamics of cross-linked actin networks. Soft Matter. 2010;6(2):218-25. doi: 10.1039/B912163N.
55. Park M, Moon RT. The planar cell-polarity gene stbm regulates cell behaviour and cell fate in vertebrate embryos. Nat Cell Biol. 2002;4(1):20-5.
56. Butler MT, Wallingford JB. Control of vertebrate core planar cell polarity protein localization and dynamics by Prickle 2. Development. 2015;142(19):3429-39. doi: 10.1242/dev.121384. PubMed PMID: 26293301.
57. Riedl J, Crevenna AH, Kessenbrock K, Yu JH, Neukirchen D, Bista M, Bradke F, Jenne D, Holak TA, Werb Z, Sixt M, Wedlich-Soldner R. Lifeact: a versatile marker to visualize F-actin. Nat Methods. 2008;5(7):605-7. Epub 2008/06/10. doi: 10.1038/nmeth.1220. PubMed PMID: 18536722; PMCID: PMC2814344.
58. Becker-Heck A, Zohn IE, Okabe N, Pollock A, Lenhart KB, Sullivan-Brown J, McSheene J, Loges NT, Olbrich H, Haeffner K, Fliegauf M, Horvath J, Reinhardt R, Nielsen KG, Marthin JK, Baktai G, Anderson KV, Geisler R, Niswander L, Omran H, Burdine RD. The coiled-coil domain containing protein CCDC40 is essential for motile cilia function and left-right axis formation. Nat Genet. 2011;43(1):79-84. doi: 10.1038/ng.727. PubMed PMID: 21131974; PMCID: PMC3132183.
59. Vielemeyer O, Nizak C, Jimenez AJ, Echard A, Goud B, Camonis J, Rain J-C, Perez F. Characterization of single chain antibody targets through yeast two hybrid. BMC Biotechnology. 2010;10(1):59. doi: 10.1186/1472-6750-10-59.
60. Schneider CA, Rasband WS, Eliceiri KW. NIH Image to ImageJ: 25 years of image analysis. Nat Methods. 2012;9(7):671-5. doi: 10.1038/nmeth.2089. PubMed PMID: 22930834; PMCID: PMC5554542.
61. Püspöki Z, Storath M, Sage D, Unser M. Transforms and Operators for Directional Bioimage Analysis: A Survey. Adv Anat Embryol Cell Biol. 2016;219:69-93. Epub 2016/05/22. doi: 10.1007/978-3-319-28549-8_3. PubMed PMID: 27207363.
62. Sbalzarini IF, Koumoutsakos P. Feature point tracking and trajectory analysis for video imaging in cell biology. J Struct Biol. 2005;151(2):182-95. doi: 10.1016/j.jsb.2005.06.002. PubMed PMID: 16043363.
63. Xu T, Langouras C, Koudehi MA, Vos BE, Wang N, Koenderink GH, Huang X, Vavylonis D. Automated Tracking of Biopolymer Growth and Network Deformation with TSOAX. Sci Rep. 2019;9(1):1717. Epub 20190208. doi: 10.1038/s41598-018-37182-6. PubMed PMID: 30737416; PMCID: PMC6368602.
64. Park TJ, Kim SK, Wallingford JB. The planar cell polarity effector protein Wdpcp (Fritz) controls epithelial cell cortex dynamics via septins and actomyosin. Biochem Biophys Res Commun. 2015;456(2):562-6. doi: 10.1016/j.bbrc.2014.11.078. PubMed PMID: 25436430; PMCID: PMC4429777.

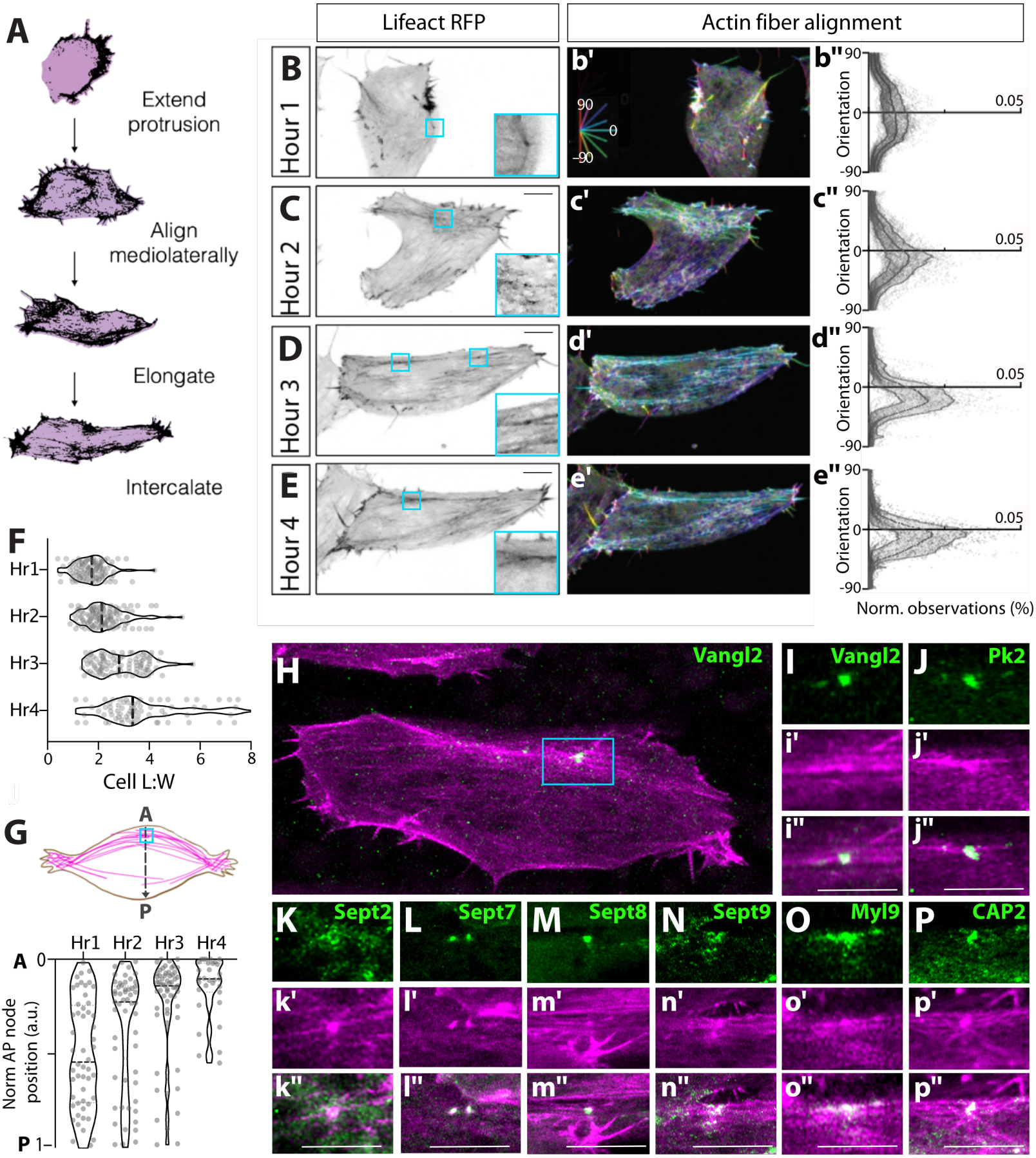

Devitt et al, Figure 1

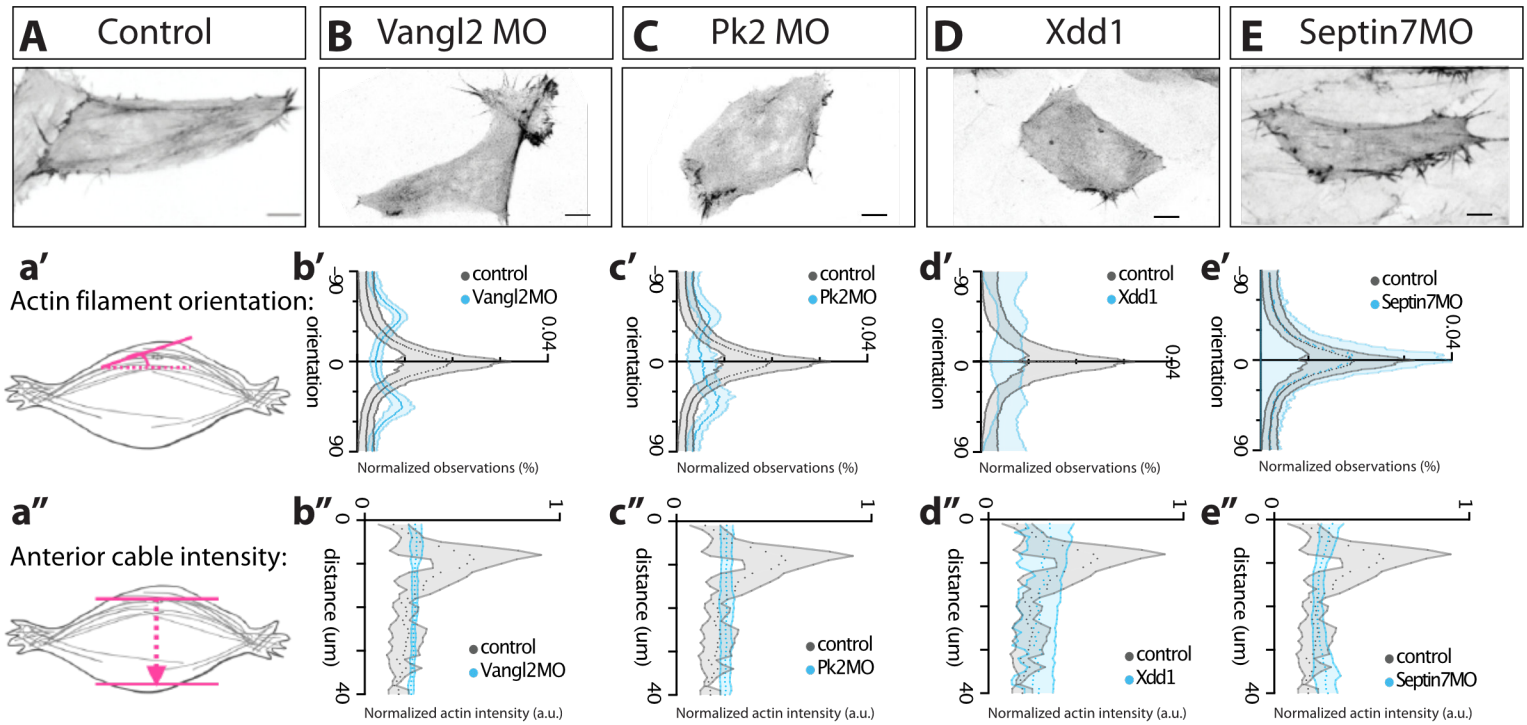

Devitt et al, Figure 2

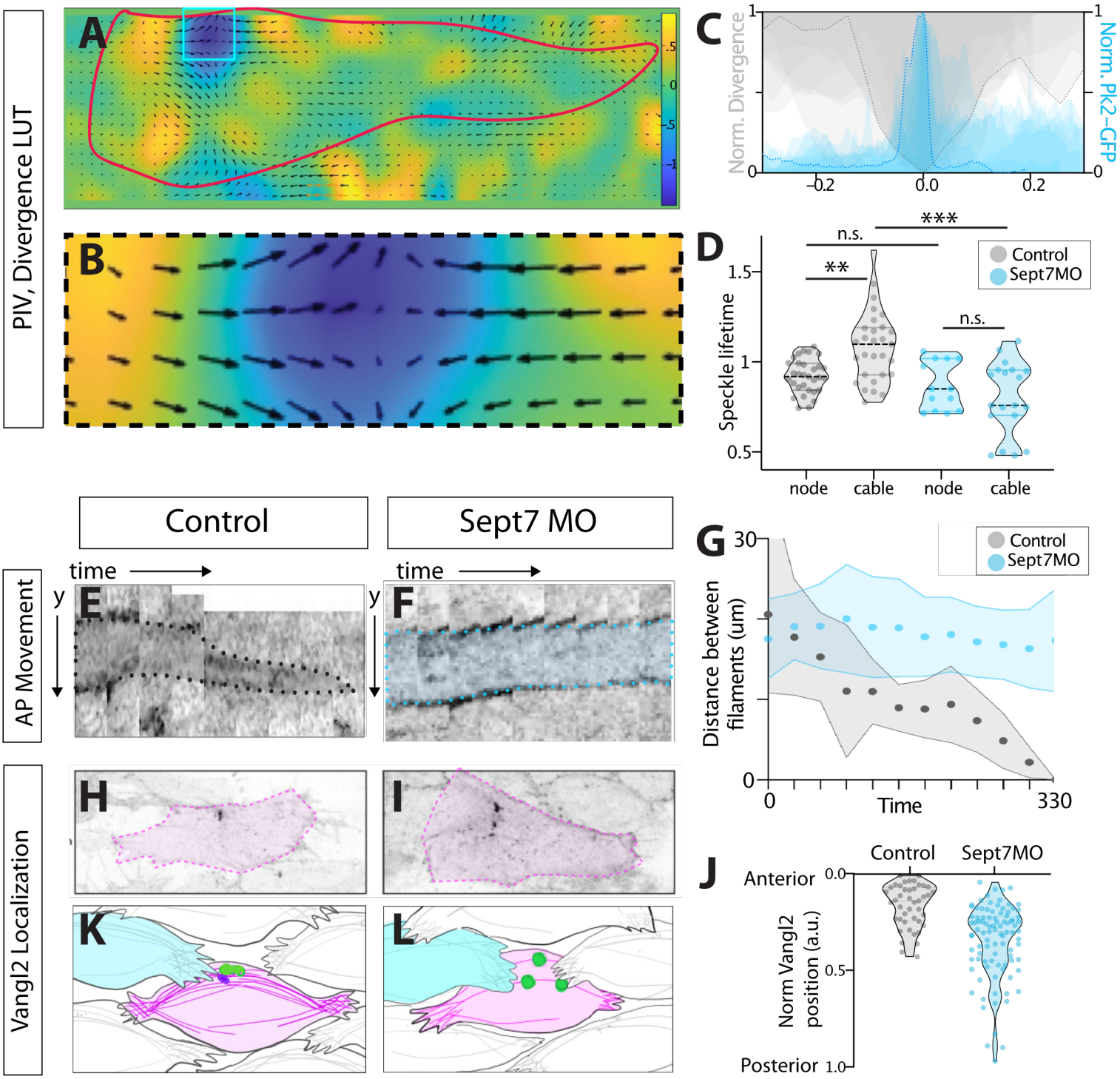

Devitt et al, Figure 3

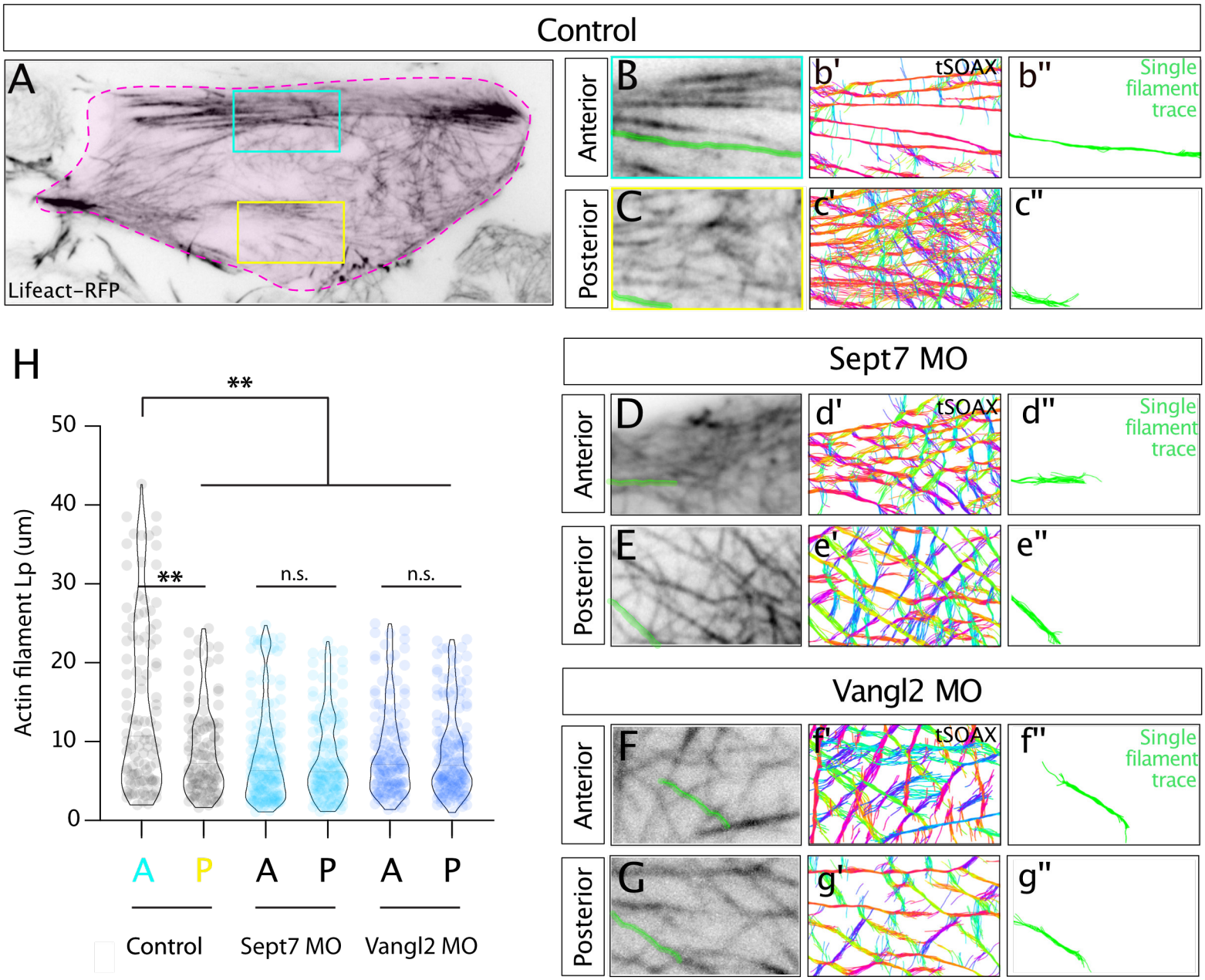

Devitt et al, Figure 4

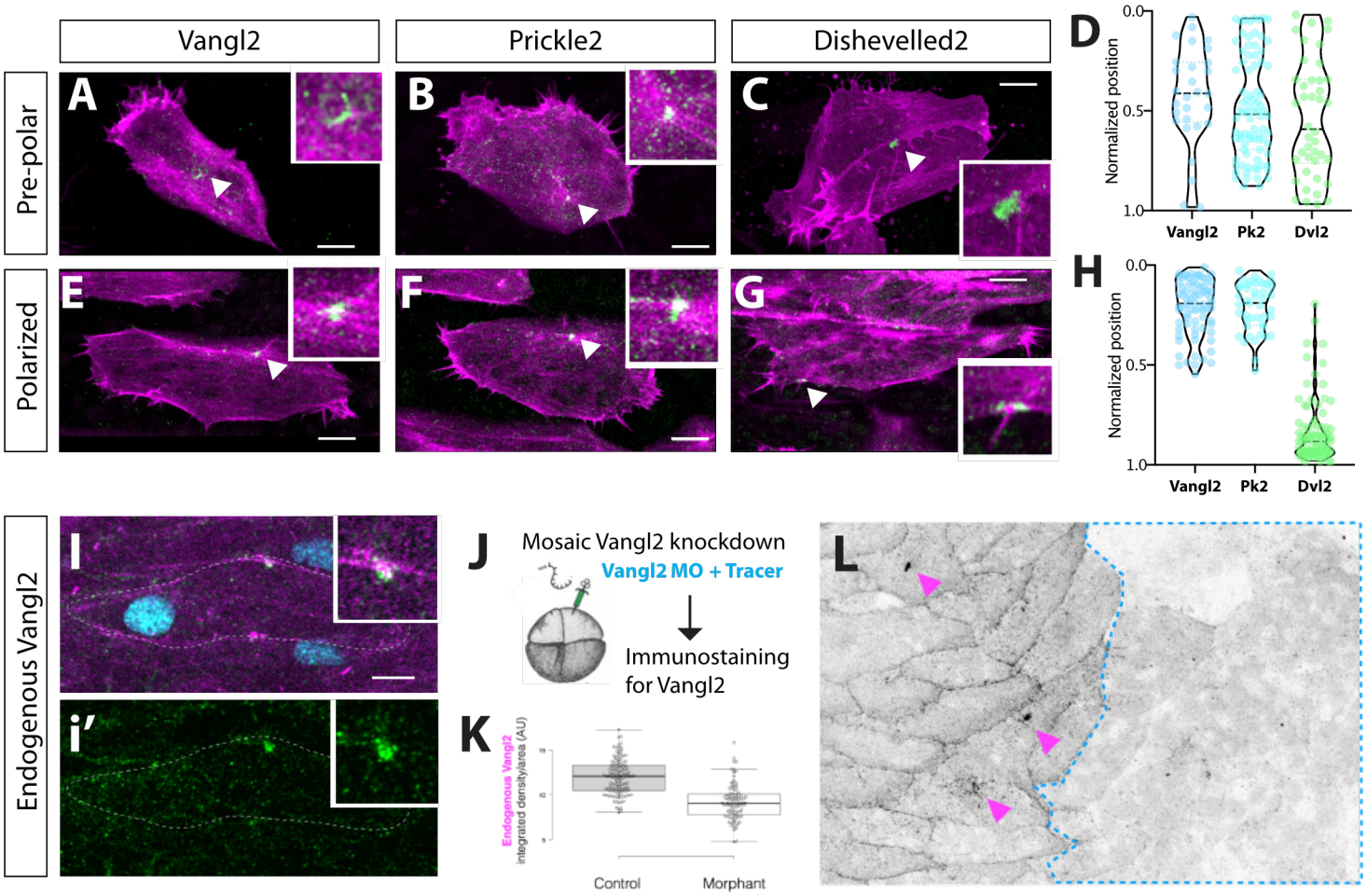

Devitt et al, Figure S1

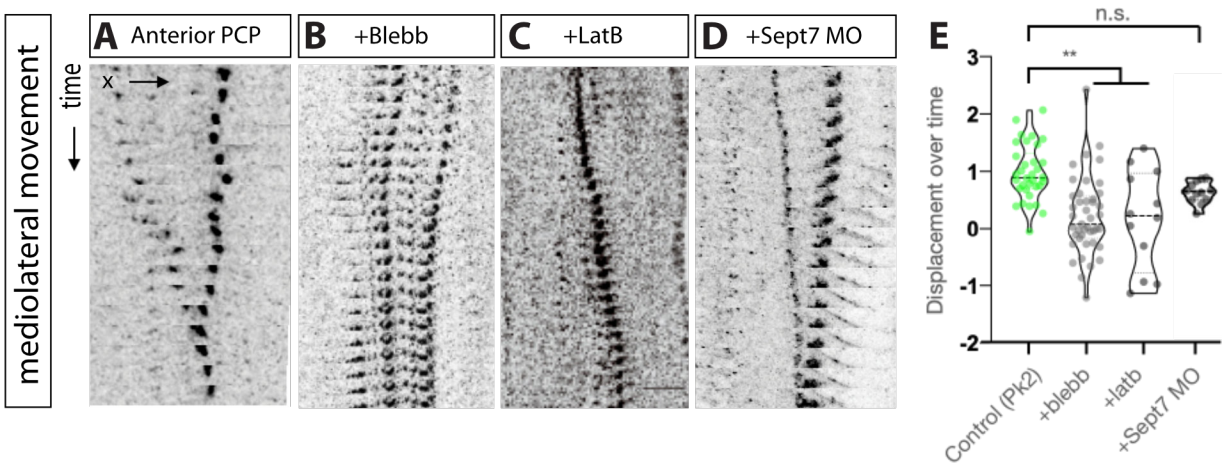

Devitt et al, Figure S2